Effect of Thermal Behavior on the Grain Morphology and Dimension of 80mm-Thick Ti6Al4V Plates Joined by Laser Melting Deposition

Feiyue Lyu
Nanjing University of Aeronautics and Astronautics
Ke Hu
Nanjing University of Aeronautics and Astronautics
Leilei Wang
Nanjing University of Aeronautics and Astronautics
Yu Feng
Nanjing University of Aeronautics and Astronautics
Xiaohong Zhan (xiaohongzhan_nuaa@126.com)
Nanjing University of Aeronautics and Astronautics

Research Article

Keywords: Laser melting deposition , Titanium alloy , Grain morphology , Grain dimension , Thermal behavior

Posted Date: July 14th, 2021

DOI: https://doi.org/10.21203/rs.3.rs-705233/v1

Effect of thermal behavior on the grain morphology and dimension of 80mm-thick Ti6Al4V plates joined by laser melting deposition

Feiyue Lyu, Ke Hu, Leilei Wang, Yu Feng, Xiaohong Zhan*

College of Materials Science and Technology, Nanjing University of Aeronautics and Astronautics, Nanjing 211106, China

*Corresponding author.

Email address: xiaohongzhan_nuaa@126.com (X. Zhan).

Abstract

Individually fabrication forged parts and then joining them together through Laser Melting Deposition (LMD) is a viable way for manufacturing large components. For investigating the effect of the grain morphology of LMD joint, two 80mm-thick Ti6Al4V plates are successfully manufactured using three different scanning speeds (10, 15, and 20 mm/s). It is essential for understanding the thermal behaviour of melt pool during LMD to improve process quality. This study focuses on the energy density of heat source and the direction of heat flux, analyzing the effect of thermal behavior on the grain morphology and dimension of deposition area, equiaxed crystal zone (EQZ) and the substrate. The macrostructure is evaluated in the different thermal condition and scanning speeds. An extremely fine equiaxed crystal was observed near the joint boundary with a high temperature gradient and cooling rate. The curve epitaxial growth of fine columnar crystal rather than along straight lines is induced by the direction of heat conduction near the joint boundary. However, the orientation angle of epitaxial growth of the coarse columnar crystal is the same as previous deposition layer at the center of deposition area. Given the effect of high heat accumulation and low temperature gradient during LMD, the dimension of columnar crystal is coarsen significantly at the center of deposition area.

Keywords Laser melting deposition · Titanium alloy · Grain morphology · Grain dimension · Thermal behavior

1 Introduction

It is widely acknowledged that the welding method were widely and successfully used to joint large-scale structures in some industrial fields such as aviation manufacture, power plants, shipbuilding, pipelines manufacture, etc [1]. High-quality welded joints have been achieved using multi-pass arc welding technology in case of thicker plates (about 140-180mm) which are used in pressure vessels [2]. However, large heat input and long cycle time of multi-pass arc welding technology give rise to significant residual stresses and accompanied post-weld distortions [3].

In contrast to conventional processing method such as multi-layer and multi-pass welding, Laser Welding with Metal Powder (LWMP) has unique and obvious advantages including a high-intensity heat source, low heat distortion, small heat affected area, fast processing efficiency and good metallurgical bonding [4-10]. Most of previous research on LWMP processes mainly concentrates on the influence of the filler material on the microstructure and the mechanical properties of the joint [11-16]. However, LWMP is only applied to join thin plates with thick of 1~5mm at present.

Large and complex components were fabricated layer-by-layer through Laser Melting Deposition (LMD) that is a near net shape additive manufacturing process [17-20]. Compared with conventional processing methods such as forging or welding, LMD technology has the unique advantage of producing and joining large-scale components [21]. Typical applications of LMD include surface modification, repair of metallic components and connection of large-scale parts in automobile, aerospace, ships domains. In the process of LMD, the joint quality depends on the thermal behavior as well as the LMD parameters such as spot size, focal position, laser power and scanning speed. Therefore, the key problem to join large-scale substrate is to control thermal behavior, which establishes a cardinal relationship between microstructure and mechanical property and in turn dictates the performance of joint.

Sun et al. [22] utilized a coaxial imaging system to observe the real-time pool characteristics in the process of LMD. The morphology of the melt pool and the cross-sectional dimension of the solidified track and grain structures of the solidified tracks were predicted under different heat inputs. Zhan et al. [23] quantitatively analysed the microstructure and associated thermal process to explore the

microcosmic mechanism during the LMD process using an Invar alloy. Subsequently, the relationship between the microstructure and thermal conditions was established using simulation and experimental work. Xiang et al. [24] applied LMD to the fabrication of CrMnFeCoNi high entropy alloys. It was reported that laser power and scanning strategy has a significant impact on CET transitions in the top region of LMD processed samples due to the effect of these parameters on heat flux direction and temperature gradient. Xu et al. [25] investigated the effect of heat input, especially by altering the laser scanning speed, on phase composition, microstructure, microhardness, residual stresses and tensile properties of the specimens. The average granular size was refined as the laser scanning speed increased. In addition, LMD processed 12CrNi2 alloy steel can meet the requirements of low alloy steel components due to the satisfactory strength and toughness.

Ti6Al4V is considered to be the "main force" of the titanium alloys due to its high specific strength, good corrosion resistance, high toughness, which is widely and successfully used in the marine, aerospace industry, etc [26-29]. Due to the large temperature gradient and rapid solidification rate during LMD, Ti6Al4V alloys are typically characterized by large columnar grains with ultrafine basket-weave microstructure, which is beneficial to mechanical properties [30-33]. To cope up with the challenges associated with the joining of large-scale titanium alloy components which are mostly used in an automotive industry, satellite launch vehicles and aircraft gas turbine engines, it seems pertinent to introduce LMD technology which can conveniently fabricate large-scale components layer by layer. However, the research results on the joining process of large-scale titanium components processed by LMD and having a thickness of around 80 mm are rarely reported.

The objective of the present research is to use LMD as a method for joining the 80mm-thick Ti6Al4V plates to explore the morphology evolution of grains from deposition area to substrate under the different thermal behavior. The change of grain dimension in deposition area, EQZ, heat affect zone (HAZ) and substrate with different heat input decided by scanning speed are quantitatively measured and analyzed. The effect of temperature gradient and solidification on grain morphology are discussed. The laser holding time and scanning speed is applied to estimate the grain dimension. The growth direction of columnar crystal under different orientation of radiation is explored.

Therefore, a research plan has been executed by exploiting Ti6Al4V titanium alloy (80mm) as a substrate and processed using LMD. The investigation has been done using different scanning speeds to understand the thermal distribution and its subsequent effect on the evolution of microstructure. The

morphology and scale of the grain structure, both in the vicinity of joint boundary and in the central region of deposition area, has been quantitively analyzed and explained in the light of temperature distribution.

2 Materials and Methods

Powder particles of Ti6Al4V having a spherical shape and diameter in the range of 80-150um were fabricated by plasma rotating electrode process (PREP). Chemical composition of the powder was shown in Table 1. Dehumidification process was executed in a vacuum furnace within which the temperature was maintained at 102℃ for 2 hours. Subsequently, the furnace was cooled to room temperature under the condition of vacuum after the insulation. Ti6Al4V base plates were first cut by Electrical Discharge Machine (EDM). After cutting, they were prepared on the milling machine to ensure the flatness and parallelism of the faying surfaces. The configuration and detailed joint design dimensions are demonstrated in Fig. 1(a) and (b). Before the LMD experiment, the faying surfaces were polished with coarser sandpaper to remove the surface oxide layer and washed with acetone.

Table 1 Chemical composition of Ti6Al4V powder.

Element	Al	V	Fe	C	N	H	O	Ti
Composition(wt.%)	5.5-6.8	3.5-4.5	0.30	0.10	0.05	0.015	0.20	Bal.

LMD system for a current experiment comprised of a 10KW fiber laser system, Argon chamber, powder feeding system with a coaxial nozzle and a motion system utilizing the KUKA robot as shown in Fig. 2. The laser beam emitted from the end of the fiber, and the measured focus spot diameter was 3 mm. A coaxial nozzle was connected to powder feeder with tube, and powder was delivered into molten pool by coaxial nozzles which were 15-20 mm above the substrate. The coaxial nozzle was mounted on a 6-axis KUKA robot. The 80mm-thick Ti6Al4V plates were jointed by LMD in a Argon chamber purged with high purity argon. Before an experiment, the Argon chamber of LMD system was cleaned and vacuum degree below 5.0×10-2 Pa was achieved. Afterwards, high purity inert gas argon was filled into the chamber which ensured the oxygen concentration in the deposition chamber to be less than 50ppm.

The molten pool was formed by irradiating the laser beam on the surface of substrate. At the same time, the Ti6Al4V powder was introduced into the molten pool at a high temperature through the powder feeding nozzle under the restriction of the powder gas. The Ti6Al4V powder melted quickly after entering the molten pool to deposit successive layers between the two Ti6Al4V plates, as is shown

in Fig 1(a) and (b). As the laser beam traversed, solidification of the molten pool initiated in the trailing half of molten pool on the surface of the previously deposited layer. Because of this multi-pass process, HAZ was also created in the already deposition layerby heat conduction. Overall schematic of this process is shown in Fig 1(c). The X-shaped groove was filled layer by layer with an overlap ratio of 50 % till the top surface of two Ti6Al4V plates. Processing parameters of LMD are listed in Table 2.

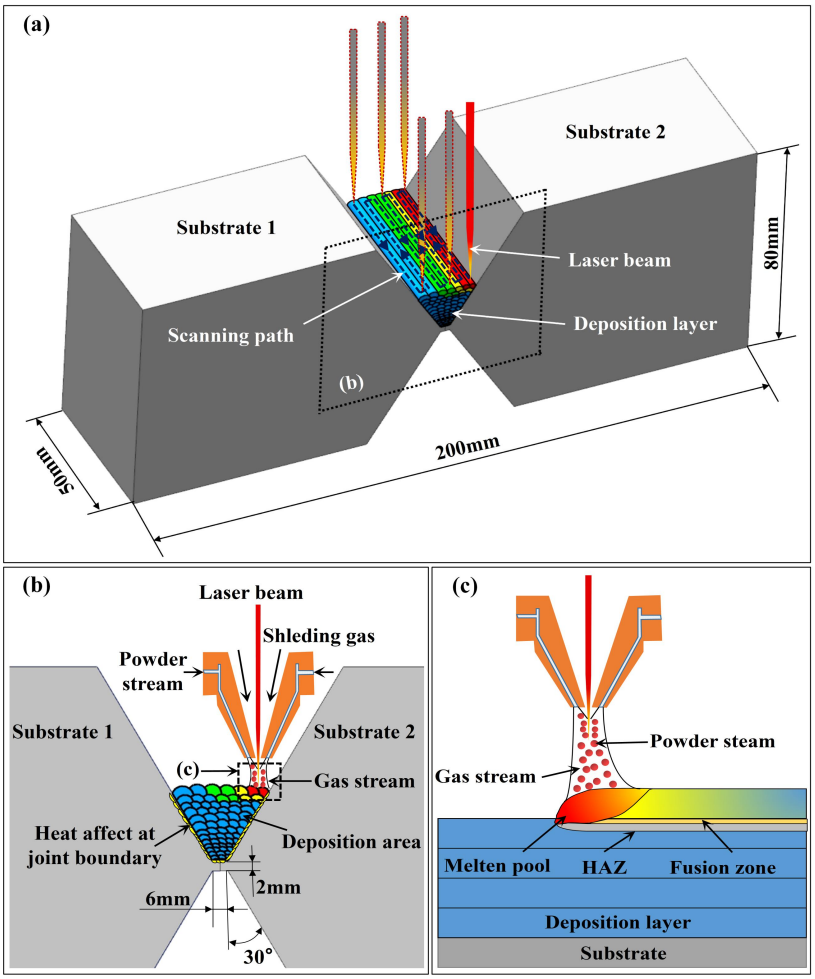

Fig. 1 (a) Isometric schematic of the LMD process (b) Transverse cross section of the LMD process (c) Longitudinal section depicting adjacent solidified layers.

Table 2 LMD processing parameters of joining Ti6Al4V titanium alloy X-shaped groove substrate.

Laser power (W)	Scanning velocity (mm/s)	Powder feeding rate (g/min)	Shielding gas flow (L/min)	Spot diameter (mm)	Overlap ratio (%)	Increment of Z (mm)
1500	10, 15, 20	8	4	3	50	0.7~1.5

In order to explore microstructural attributes, samples were extracted from the joint boundary to the central region of deposition area. These samples were ground with progressively increasing abrasive papers upto 2000# and then polished with a diamond abrading agent having a particle size of

1μm. Thereafter, these samples were etched by the Kroll reagent (4mL HNO3 + 2mL HF + 100mL H2O). Grain structure was recorded by the stereomicroscope, which is used for analyzing the apparent grain morphology and characteristic scale evolution between the joint boundary and the center of deposition area. In addition, the grain dimension transformation in the different regions was analyzed and contrasted under different scanning speeds.

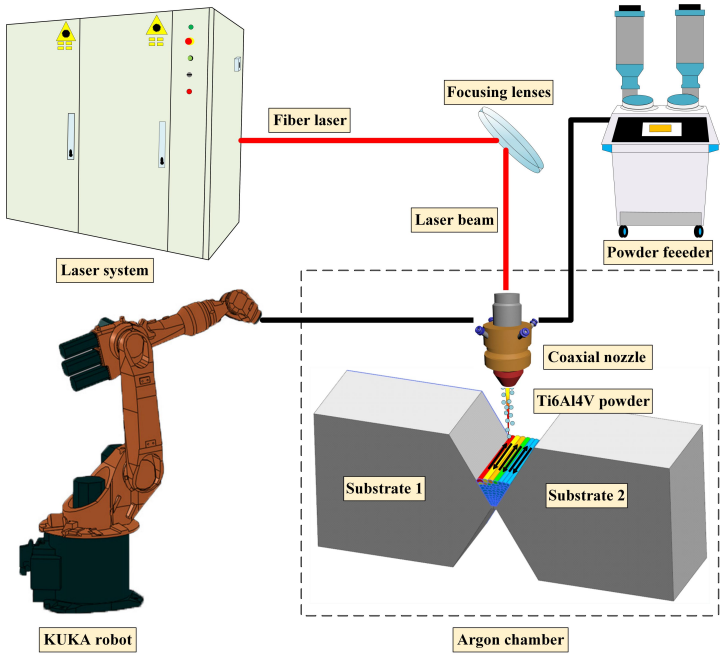

Fig. 2 Schematic diagram of equipment in the experiment.

3 Results and discussion

3.1 Relationship between grain morphology and temperature distribution

Fig. 3 shows the influence of thermal behavior on the macromorphology of LMD joint when the laser power is 1500W and the scanning speed is 10mm/s. Equiaxed crystal zone (EQZ) is observed near the joint boundary in Fig 3(b) and the average width of EQZ is 2.06mm in Fig 3(d). Quantitative characterization of the average size of an equiaxed crystal in EQZ is done through measuring software. The feature of distribution of grain diameters shows the normal distribution, and the average grain diameter is 0.27mm as can be seen in Fig. 3(e). After that, an epitaxial growth of fine columnar crystal takes place by obvious phenomenon of heterogeneous nucleation aided by already existing equiaxed crystals as shown in Fig. 3(b). The sidewall of joint boundary is peculiarly prone to conduct heat rapidly, inducing a rapid increase of undercooling degree for nucleation. It could be explained by the fact that the relatively higher undercooling degree promotes nucleation rate, leading to the formation of more refined grain near the sidewall of X-shaped groove. However, columnar crystals coarsen

significantly at the middle deposition layer of X-shaped groove. It can be speculated that the phenomenon of heat accumulation at the middle deposition layer of X-shaped groove facilitates the growth of coarser columnar crystal shown in Fig. 3(c).

Details of the the shape of molten pool and energy density of Gauss heat source during LMD process are published in Fig. 4(a) and (b). In Fig. 4(b), it is found the maximum value of heat flux exists at node 1 and given as 2.12×107W/m2. The general expression for the heat flux q is calculated as follows:

$$q = \alpha_p \cdot P \cdot \frac{1}{\sigma\sqrt{2\pi}} e^{\frac{-(x-x_0)^2}{2\sigma^2}} \cdot \frac{1}{\sigma\sqrt{2\pi}} e^{\frac{-(y-y_0)^2}{2\sigma^2}} \quad (1)$$

Where α_p is powder absorptivity, P is the laser power, σ is the Gaussian distribution function taken as a quarter of the laser spot diameter. The laser spot diameter is 3mm in this experiment. Initial location of the coordinate system is given by x0 and y0 while the main field spatial variables are x and y. During LMD process, the deposition powder and surface of substrates are melted. The surface of substrates forms an ellipsoidal shape molten pool under the effect of Gaussian heat source distribution. The elongated shape of the molten pool could be attributed to the higher laser scanning speed, as shown in Fig. 4(a).

Fig. 4(c) shows the temperature distribution curve around the molten pool when the laser power is 1500W and the scanning speed is 10mm/s. The process of single-track laser melting at the surface of substrates is created by the model which explains the evolution of grain morphology and dimension at LMD joint under the effect of temperature distribution. The temperature in the center of molten pool (Node 1) is about 2004.68℃. As the distance from the center of the molten pool increasing to 0.2mm, the temperature reduces to 1515.52℃ at Node 2. In addition, the temperature around the HAZ changes from 883.30℃ (Node 3) to 475.88℃ (Node 4), which lies in the range between 0.5mm and 1.0mm from the center of molten pool. Therefore, there exists sharp temperature gradients which gives rise to higher undercooling level in the vicinity of HAZ, thus facilitating the conditions for the formation of fine grains around the joint boundary. Therefore, there exists sharp temperature gradients which gives rise to higher undercooling level in the vicinity of HAZ, thus facilitating the conditions for the formation of fine grains around the joint boundary. However, coarser columnar crystals are formed easily after the solidification of molten pool because of the low-temperature gradient and undercooling

level at the center of deposition area. Finally, at a distance exceeding 3 mm from the molten pool center, temperature keeps stable at 25℃ (Node 5).

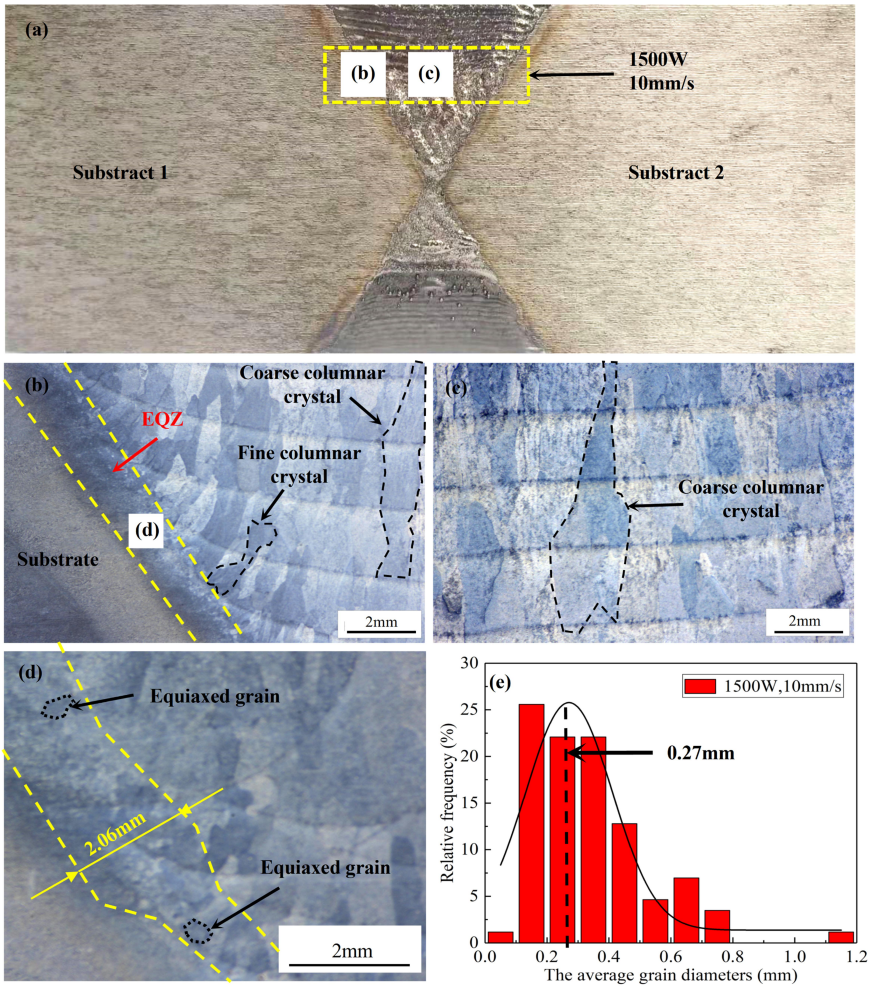

Fig. 3 The effect of temperature distribution on the macro morphology with laser power at 1500W and scanning speed at 10mm/s after the LMD process. (a) macromorphology of LMD joint; (b) micro morphology of LMD sample at joint boundary; (c) micro morphology LMD sample at the center of deposition area; (d) magnified view of EQZ; (e) the Gaussian distribution of equiaxed grains in EQZ.

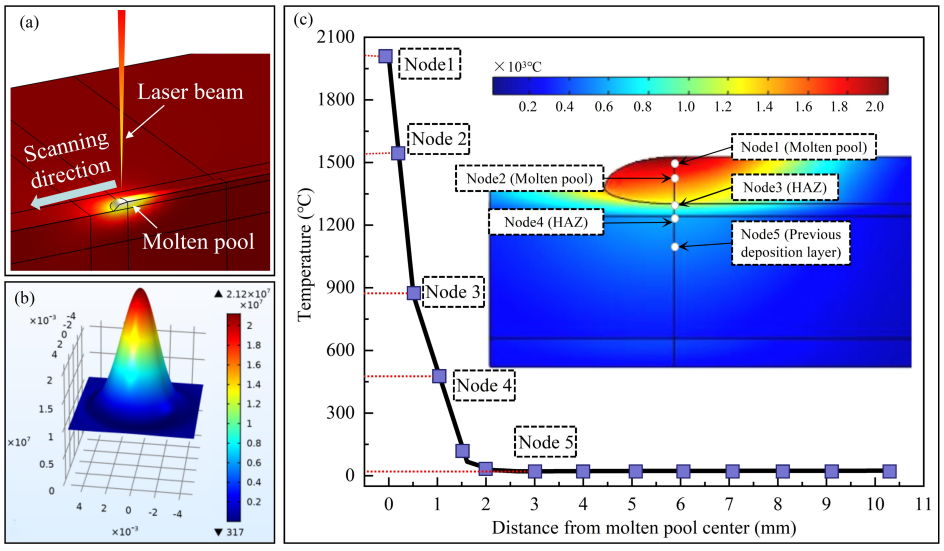

Fig. 4 (a) The shape of molten pool during the process of LMD; (b) Energy density of Gauss heat source in the process of LMD; (c) The temperature distribution curve around the molten pool when the laser power is 1500W and the scanning speed is 10mm/s.

The process of grain morphology transition from β-equiaxed crystal at EQZ to β-columnar crystal at LMD joint are presented in Fig. 5(a). Both Nucleation rate (N) and Growth rate (G) of the grains are generally considered as being proportional to the undercooling level which decreases as the S/L interface advances towards the central region of molten pool [34]. However, the value of N/G of grains are negative (N/G<0) at the center of deposition area which reduces the number of grains per unit volume ZV. The relationship between ZV and N/G is depicted by Eq. (2).

$$Z_V = 0.9\left(\frac{N}{G}\right)^{\frac{3}{4}} \tag{2}$$

When the value of N/G of grains are positive (N/G>0), columnar crystals tend to be finer as the undercooling is high close to the joint boundary. In addition, a large number of fine equiaxed crystal are formed at EQZ due to a high undercooling degree when the value of nucleation rate (N) far exceeds the growth rate (G).

Fig 5(b) shows that the "component supercooling" zone starts to appear when the actual temperature gradient (Tq) in the liquid phase ahead of the solid liquid interface is less than the liquidus temperature gradient (TL) given by the phase diagram of concerned material. When the growth condition of the plane interface is destroyed, cellular or dendritic structure begin to grow due to the formation of composition undercooling. The main factors affecting the composition supercooling of Ti6Al4V alloy are the original composition C0, the temperature gradient GL and the solidification rate R of the liquid phase. Meanwhile, the growth morphology of crystals are influenced by these factors directly. As is shown in Fig. 5(c), the crystal morphology changes from planar crystal to dendritic under the condition of constant C0 with the decrease of $G_L/\sqrt{R}$. According to Eq. (3), it is also found that the maximum "component supercooling" degree ($\Delta T_{\max}$) increases significantly when the value of GL/R goes down, which is beneficial which is beneficial for forming dendrites at the deposition area. The maximum "component supercooling" ($\Delta T_{\max}$) can be presented by Eq. (3) [34]:

$$\Delta T_{\max} = \frac{m_L C_0 (1-k_0)}{k_0} - \frac{G_L D_L}{v}\left[1 + \ln\frac{v m_L C_0 (1-k_0)}{G_L D_L k_0}\right] \tag{3}$$

Where DL is solute diffusion coefficient in liquid phase, GL is the actual temperature gradient, v is migration velocity of solid/liquid interface, mL is the slope of liquidus and k0 is solute partition

coefficient.

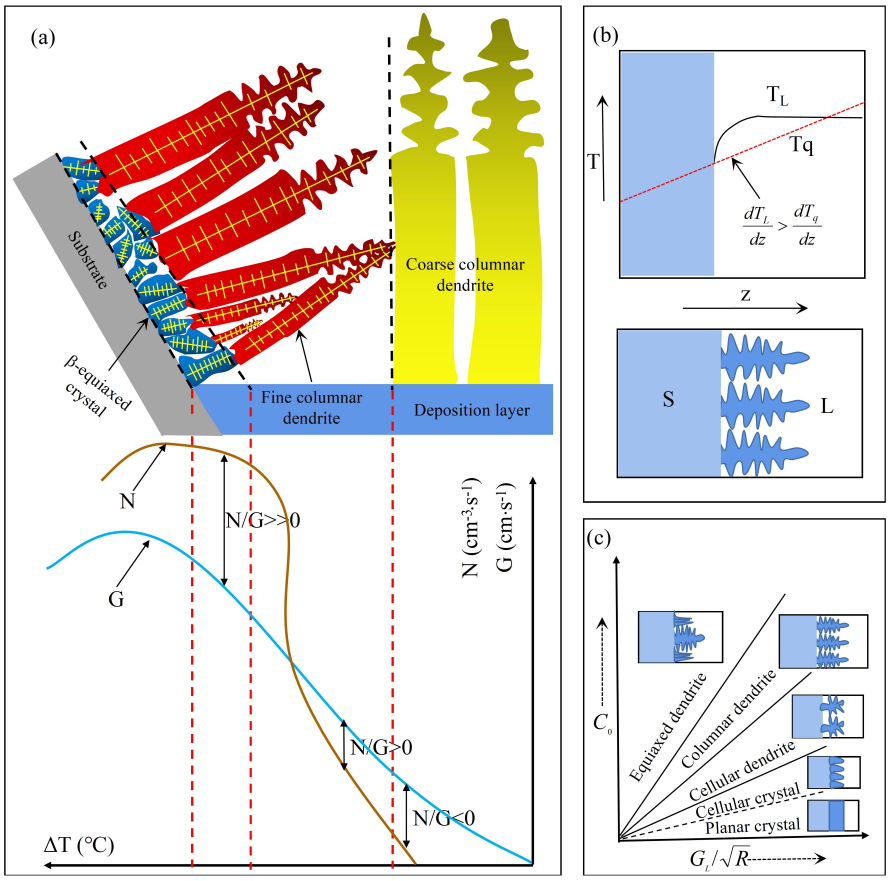

Fig. 5 (a) The relationship between undercooling and the ratio of nucleation rate and growth rate of metals during crystallization; (b) The relationship between composition supercooling and solid-liquid interface morphology; (c) Effect of C0 and $G_L/\sqrt{R}$ on crystal morphology of solid solution.

3.2 Effects of thermal behavior on grain dimension and growth direction

The heat input, temperature gradient and cooling rate are depended on laser scanning speed in the process of LMD. The width of EQZ become narrow with the increasing of scanning speed compared Fig. 3(c) with Fig. 6(a), (e). It is obtained that the average width of EQZ is about 2.06mm in Fig. 3(c) when the laser power is 1500W and the scanning speed is 10mm/s. In contrast, the average width of EQZ is only 1.58mm and 1.41mm respectively when the scanning speed increases to 15mm/s and 20mm/s respectively in Fig. 6(a) and (e). At scanning speed of 20mm/s, the width of EQZ is approximately 32 % lesser than that of what exists at 10mm/s. This fact could be attributed to the lower local heat input which creates higher temperature gradients and refines the grain structure in the vicinity of joint boundary.

The frequency histogram with its gaussian distribution is applied to analyze the size of equiaxed crystal in EQZ under the influence of different scanning speeds in Fig. 6(c) and (g). Results show that

the average grain diameter of equiaxed crystal follows a normal distribution in EQZ. The peak value of gaussian distribution curve is shifted to the left which indicates that the average grain diameter of equiaxed crystal goes down as the scanning speed is increasing, as revealed in Fig. 3(c) and Fig. 6(c), (g). To be specific, the average grain diameter is about 0.27mm when the laser power is 1500W and the scanning speed is 10mm/s. As the scanning speed is increased up to 15 and 20mm/s, the average grain diameter goes down to 0.21 and 0.18mm because of an obvious reduction in heat input. Similar trend can be observed in the microstructural morphology in the central region as displayed in Fig. 6(b) and Fig. 6(f). It can be noticed that the aspect ratio of columnar crystals decreases as the speed is increased from 15mm/s to 20mm/s.

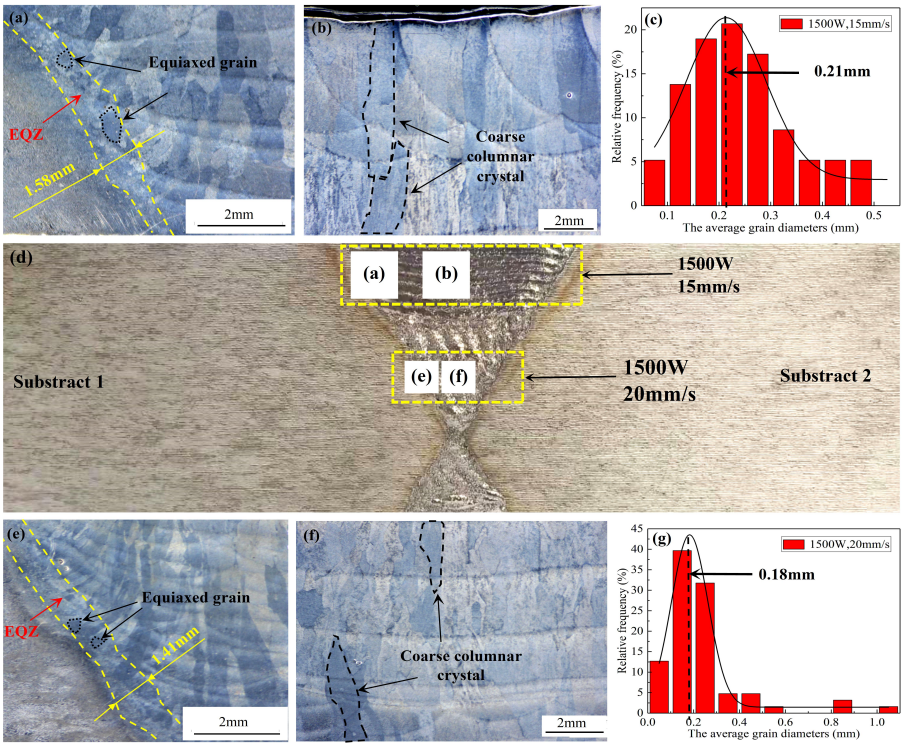

Fig. 6 Effect of temperature distribution on the microstructure evolution with scanning speeds of 15mm/s and 20mm/s when the laser power is at 1500W. (a) micro morphology of LMD sample at joint boundary at 15mm/s; (b) micro morphology LMD sample at the center of deposition area at 15mm/s; (c) gaussian distribution of equiaxed grains in EQZ at 15mm/s; (d) macro morphology of LMD joint; (e) micro morphology of LMD sample at joint boundary at 20mm/s; (f) micro morphology LMD sample at the center of deposition area at 20mm/s; (g) gaussian distribution of equiaxed grains in EQZ at 20mm/s.

Fig. 7 confirms that the influence of scanning speed on the dimension of fine columnar crystals at the joint boundary. With the scanning speed increasing from 10 to 20mm/s, the length of the fine columnar crystals decreases from 1.02mm to 0.55mm due to an obvious reduction in local heat input and concomitant increase in cooling rate. However, scanning speed has no significant impact on the

width of fine columnar crystals which always keep stable at about 0.21mm. However, unlike finer columnar crystals, the width of coarse columnar crystals at the central region demonstrated a continuous downward trend as the speed was increased from 10 to 20 mm/s in Fig. 8(b). The average width of coarse columnar crystal is 1.03mm for 10mm/s which is quite similar to the width of fine columnar crystal in the vicinity of joint boundary (see Fig. 8c). However, the width of coarse columnar crystal is reduced by 17.5% when the scanning speed is increased to 15mm/s (see Fig. 8d). Most significant reduction of more than 50% in the width of coarse columnar crystals is achieved with a speed of 20 mm/s, as shown in Fig. 8(e). However, the accurate length of coarse columnar crystals is difficult to obtain because view goes beyond the range of stereomicroscope.

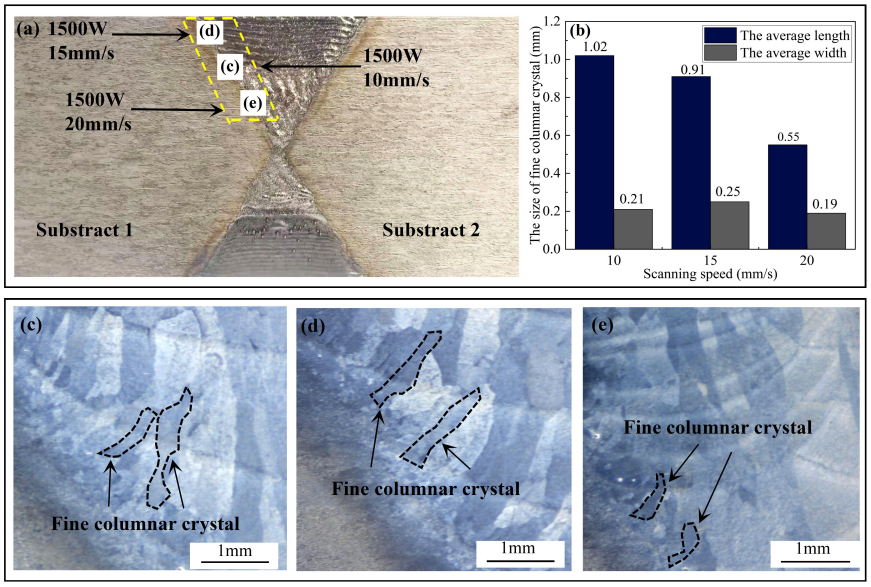

Fig. 7 Quantitative measurement of fine columnar crystal dimension with different scanning speeds at the joint boundary. (a) macro morphology of LMD joint; (b) variation of fine columnar size with scanning speed; (c) micro morphology of fine columnar crystal with the scanning speed of 10mm/s; (d) 15mm/s and (e) 20mm/s..

There is a special relationship between the temperature of molten pool and laser scanning speed during the process of LMD. The analytical expression of the temperature of molten pool can be summarized as follows [35]:

$$T(r,x)=\frac{AP}{2\pi kr}\exp\left(-\frac{Vr}{2\alpha}-\frac{Vx}{2\alpha}\right) \tag{4}$$

Where A is the absorption coefficient because feeding power can absorb part of laser, P is the laser power, k is the thermal conductivity, α is the thermal diffusivity, r is the distance between the origin of the moving coordinate and the calculation point, x is coordinates of calculation points and V is the laser scanning speed. Therefore, it can be identified the temperature of molten pool T(r,x) is rising with the

laser scanning speed v decreasing.

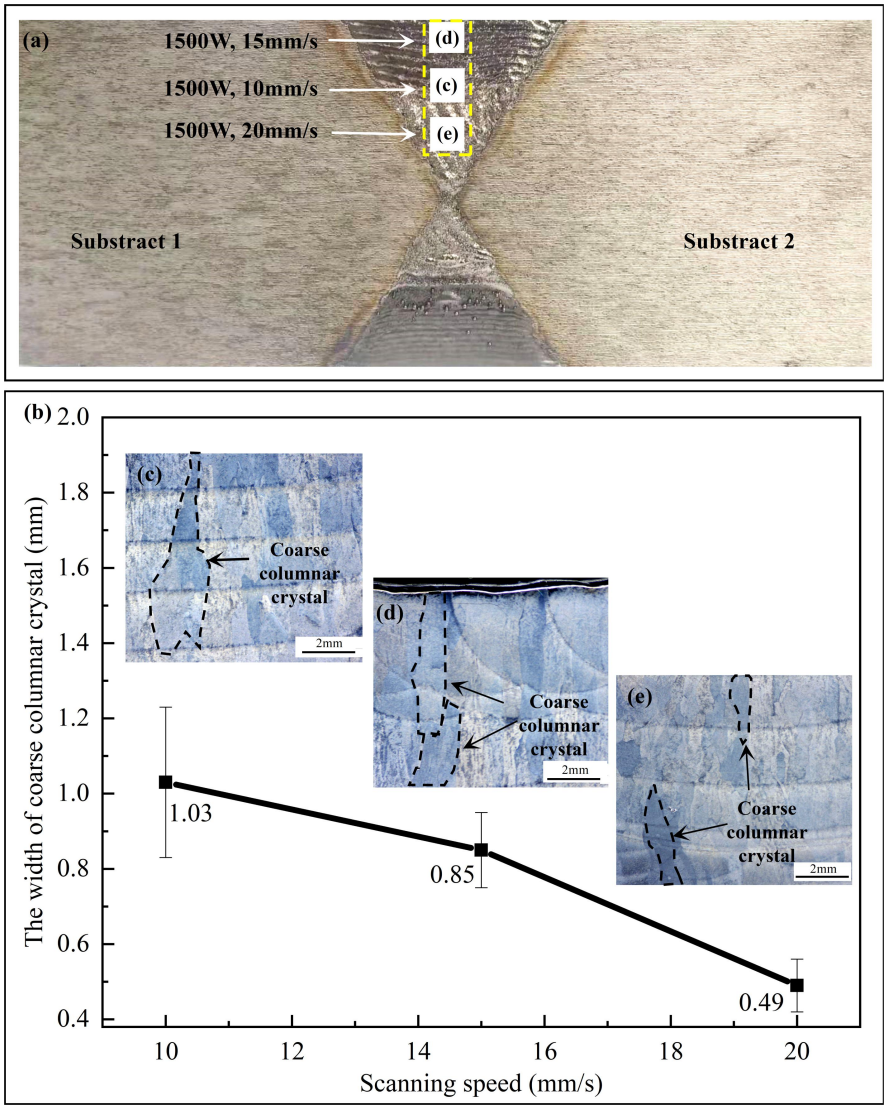

Fig. 8 Quantitative measurement of coarse columnar crystal dimension with different scanning speeds in the center of deposition area.(a) macro morphology of LMD joint depicting areas with different scanning speeds; (b) variation of the width of coarse columnar crystal with relevant scanning speed; (c) the macro morphology of coarse columnar crystal with the scanning speed at 10mm/s; (d) the macro morphology of coarse columnar crystal with the scanning speed at 15mm/s; (e) the macro morphology of coarse columnar crystal with the scanning speed at 20mm/s.

In order to explore grain growth kinetics of fine columnar crystal near the joint boundary during LMD process, a classical grain growth kinetics equation was used [36]:

$$G^n - G_0^n = K_0 t \exp\left(-\frac{Q}{RT}\right) \tag{5}$$

Where G is the average grain dimension of columnar crystal, G0 is the grain size of substrate, n is the grain growth kinetic exponent, K0 is a constant, t is the holding time of laser at a position, R is an ideal gas constant at 8.314J/(mol·K), T is absolute temperature, Q is the grain growth activation energy.

Due to the larger dimension of grain in deposition than that in the substrate (G>>G0), G0 can be neglected. Therefore, the equation (5) can be simplified as:

$$\lg G = \frac{1}{n}\lg t + \frac{1}{n}\left(\lg K_0 - 0.434\frac{Q}{RT}\right) \tag{6}$$

When the laser scanning speed is increasing, the laser holding time t is shortened and the average grain dimension of columnar crystal is decreased according to the equation (6).

Moreover, when the holding time t is constant, the equation (5) can be simplified as:

$$\lg\frac{G^n}{t} = \left(-0.434\frac{Q}{R}\right)T^{-1} + \lg K_0 \tag{7}$$

According to equation (7), the grain dimension of columnar crystal G goes rising when the laser holding time is prolonged, which means the laser scanning speed is low at this time.

In addition, the dimension of columnar crystal is coarser in the center of the deposition layer due to heat accumulation. Considering the low temperature gradient andcooling rate, the large columnar grains continue to grow during solidification. The growth direction of coarse columnar crystal is determined by the heat-extraction direction (Qv), which is perpendicular to the molten-pool profile, as is shown in Fig. 9. The fine columnar crystals are grown along the orientation of radiation (Qv) which is perpendicular to sidewalls of the X-shaped groove. Curved growth of fine columnar crystal can also take place shown in Fig. 9(b). It can be explaied that the growth direction of fine columnar crystals are perpendicular to sidewall of the X-shaped groove, which grow along the opposite direction of heat dissipation. After that, the fine columnar crystal changes to another growth direction which is perpendicular to the molten-pool profile. Therefore, the reason for curved growth of fine columnar crystal is relevant to the orientation of radiation (Qv).

For curved growth phenomenon, the orientation angle has already changed because of the different direction of the molten-pool profile and Qv between the joint boundary and the center of deposition layer [34]. However, the orientation angle of the epitaxial growth of the coarse columnar crystal is the same as that of the previous deposition layer in the center of the deposition area shown in Fig. 9(c). The direction of Qv is always perpendicular to horizontal plane. The epitaxial growth of coarse columnar crystal along straight lines is induced by the direction of Qv in the center of the deposition area.

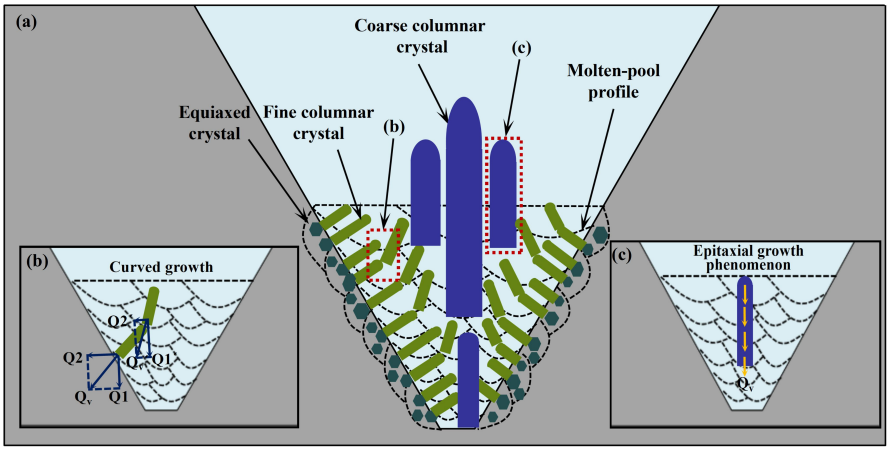

Fig. 9 Schematic diagram of columnar crystal growth for Ti6Al4V thick plates in the process of LMD.

4 Conclusions

In the present study, Ti6Al4V titanium alloy thick plates (80mm) has been joined through a LMD method by adopting different laser scanning speeds. The micromorphology of grains in relation to different local heat distribution due to varying heat input has been investigated. The main findings can be summarized as follows:

(1) Equiaxed crystal is formed in the EQZ near the joint boundary because of the high undercooling level. Epitaxial growth of fine columnar crystals grows on the equiaxed crystals in the process of LMD. The fine columnar crystal becomes coarser significantly at the center of deposition area due to the effect of heat accumulation, which is located at the middle deposition layer of X-shaped groove. It can be seen that there is different temperature distribution in different positions on the Ti6Al4V plates which accounts for different grain morphology.

(2) Quantitative measurement of the equiaxed crystal size and the width of equiaxed crystal zone at different scanning speeds was executed by commercial software. The average grain diameter of equiaxed crystal follows a normal distribution in the equiaxed crystal zone. As the scanning speed is increased, the average grain diameter declines slightly because of the decrease of heat input during LMD operation.

(3) Quantitative measurement of the length and width of fine columnar crystal at the joint boundary revealed that they possess an inverse relationship with the scanning speed which causes a decrease in the heat input decreasing and an increase in cooling rate. However, scanning speed has no significant effects on the width of fine columnar crystals. Meanwhile, the width of coarse columnar crystal in the center of deposition area is reduced by 17.5% with the scanning speed rising from 10mm/s to 15mm/s. When the scanning speed continues to increase to 20mm/s, the width reduction of

coarse columnar crystal is more than 50%..

(4) Due to the effect of undercooling level in different regions of the LMD joint, a large number of fine equiaxed crystals are formed in EQZ. A fine columnar crystal grows epitaxially from the fine equiaxed crystals in EQZ. Then the fine columnar crystal changes another direction continuing to grow along the direction of Qv which is perpendicular to the molten-pool profile. However, at the center of deposition area, the ratio of Nucleation rate and Growth rate is negative, which means the coarse columnar crystals can be formed in this region, and the orientation angle of epitaxial growth of the coarse columnar crystals are same as before at the center of deposition area.

Declarations

Funding

This work was supported by the National Science Foundation of China under Grant [51975285].

Conflicts of interest

The authors declare that they have no known competing financial interests or personal relationships that could have appeared to influence the work reported in this paper.

Availability of data and material

The raw/processed data required to reproduce these findings cannot be shared at this time as the data also forms part of an ongoing study.

Code availability

No supplementary code available.

Authors' contributions

Feiyue Lyu: Investigation, Data curation, Formal analysis, Writing – original draft. Ke Hu: Methodology, Writing – review & editing. Leilei Wang: Writing – review & editing, Validation. Feng Yu: Resources, Data curation. Xiaohong Zhan: Conceptualization, Supervision.

References

[1] Zhang XD, Eiji A, Shoh T, Yusuke A, Masaya O, Seiji K, Masami M (2011) Welding of thick stainless steel plates up to 50 mm with high brightness lasers. J Laser Appl 23:22002. https://doi.org/10.2351/1.3567961

[2] Feng J, Guo W, Francis J, Irvine N, Li L (2016) Narrow gap laser welding for potential nuclear pressure vessel manufacture. J Laser Appl 28:022421. https://doi.org/10.2351/1.4943905

[3] Yang WX, Xin JJ, Fang C, Dai WH, Wei J, Wu JF, Song YT (2018) Microstructure and mechanical properties of ultra-Narrow gap laser weld joint of 100 mm-thick SUS304 steel plates. J Mater Process Tech 265:130-137. https://doi.org/10.1016/j.jmatprotec.10.017

[4] Harooni M, Carlson B, Strohmeier BR, Kovacevic R, Gao XD (2014) Pore formation mechanism and its mitigation in laser welding of AZ31B magnesium alloy in lap joint configuration. Mater Des 58:265-276. https://doi.org/10.1016/j.matdes.2014.01.050

[5] Khan MA, Romoli L, Dini G (2013) Laser beam welding of dissimilar Ferritic/Martensitic stainless steel in a butt joint configuration. Opt Laser Technol 49:125-136. https://doi.org/10.1016/j.optlastec.2012.12.025

[6] Zhang SH, Shen YF, Qiu HJ (2013) The Technology and Welding Joint Properties of Hybrid Laser-TIG Welding on Thich Plate. Opt Laser Technol 48:382-388. https://doi.org/10.1016/10.1016/j.optlastec.2012.11.014

[7] Oliveira JP, Panton B, Zeng Z, Omori T, Zhou Y, Miranda RM, Braz FM (2016) Laser welded superelastic Cu-Al-Mn shape memory alloy wires. Mater Des 90:122-128. https://doi.org/10.1016/j.matdes.2015.10.125

[8] Sun XF, Shehab E, Mehnen J (2013) Knowledge modeling for laser beam welding in the aircraft industry. Int J Adv Manuf Tech 66:763-774. https://doi.org/10.1007/s00170-012-4364-0

[9] Sathiya P, Abdul Jaleel MY, Katherasan D, Shanmugarajan B (2011) Optimization of laser butt welding parameters with multiple performance characteristics. Opt Laser Technol 43:660-673. https://doi.org/10.1016/j.optlastec.2010.09.007

[10] YangYS, Lee SH (1999) A study on the joining strength of laser spot welding for automotive applications. J Mater Process Tech 94:151-156. https://doi.org/10.1016/S0924-0136(99)00094-1

[11] Errico V, Campanelli SL, Angelastro A, Mazzarisi M, Casalino G (2020) On the feasibility of AISI 304 stainless steel laser welding with metal powder. J Manuf Process 56:96-105. https://doi.org/10.1016/j.jmapro.2020.04.065

[12] Ju H, Lin C, Liu Z, Zhang JQ (2018) Study of In-situ formation of Fe-Mn-Si shape memory alloy welding seam by laser welding with filler powder. Opt Laser Technol 104:65-72. https://doi.org/10.1016/j.optlastec.2018.01.062

[13] Xia H, Zhang L, Tan C, Wu LJ, Chen B, Li LQ (2019) Effect of heat input on a laser powder deposited Al/steel butt joint. Opt Laser Technol 111:459-469. https://doi.org/10.1016/j.optlastec.2018.10.032

[14] Li LQ, Xia HB, Tan CW, Ma NS (2018) Effect of groove shape on laser welding-brazing Al to steel. J Mater Process Tech 252:573-581. https://doi.org/10.1016/j.jmatprotec.2017.10.025

[15] Sun JL, Yan Q, Li ZG, Huang J (2016) Effect of Bevel Angle on Microstructure and Mechanical Property of Al/steel Butt Joint Using Laser Welding–Brazing Method. Mater Des 9:468-477. https://doi.org/10.1016/j.matdes.2015.10.154

[16] Jacques L, Ouafi AE (2017) Experimental investigation of laser welding process in butt-joint configurations. World Journal of Engineering & Technology 5:77-89. https://doi.org/10.4236/wjet.2017.51007

[17] Lei ZL, Tian Z, Li P, Chen YB, Zhang HQ, Gu JY, Su X (2017) Effect of Si content on microstructure and thermo-physical properties of the joint of Sip/6063Al composite by laser melting deposition. Opt Laser Technol 97:116-123. https://doi.org/10.1016/j.optlastec.2017.06.019

[18] Kobryn PA, Moore EH, Semiatin SL (2000) The effect of laser power and traverse speed on microstructure, porosity, and build height in laser-deposited Ti-6Al-4V. Scr Mater 43:299-305. https://doi.org/10.1016/S1359-6462(00)00408-5

[19] Kobryn A, Semiatin SL (2001) The Laser Additive Manufacture of Ti-6Al-4V. JOM 53:40-42. https://doi.org/10.1007/s11837-001-0068-x

[20] Liu CM, Tian XJ, Tang HB, Wang HM (2013) Microstructural characterization of laser melting deposited Ti-5Al-5Mo-5V-1Cr-1Fe near β titanium alloy. J Alloys Comp 572:17-24. https://doi.org/10.1016/j.jallcom.2013.03.243

[21] Wang Y, Tang H, Fang Y, Wang H (2013) Microstructure and mechanical properties of hybrid fabricated 1Cr12Ni2WMoVNb steel by laser melting deposition. Chin J Aeronaut 26:481-486. https://doi.org/10.1016/j.cja.2013.02.027

[22] Sun Z, Guo W, Li L (2020) In-process measurement of melt pool cross-sectional geometry and grain orientation in a laser directed energy deposition additive manufacturing process. Opt Laser Technol 129:106208. https://doi.org/10.1016/j.optlastec.2020.106280

[23] Zhan XH, Meng Y, Zhou JJ, Qi CQ, Zhang CL, Gu DD (2018) Quantitative research on microstructure and thermal physical mechanism in laser melting deposition for Invar alloy. J Manuf Process 31:221-231. https://doi.org/10.1016/j.jmapro.2017.11.018

[24] Xiang S, Li JF, Luan HW, Amar A, Lu S, Li K, Zhang L, Liu X, Le GM, Wang XY, Qu FS, Wang D, Li Q (2019) Effects of process parameters on microstructures and tensile properties of laser melting deposited CrMnFeCoNi high entropy alloys. Mater Sci Eng A 743(16):412-417.

https://doi.org/10.1016/j.msea.2018.11.110

[25] Xu YH, Zhang CH, Zhang S, Qiao RQ, Zhang JB, Abdullah AO (2020) Scanning velocity influence on microstructure evolution and mechanical properties of laser melting deposited 12CrNi2 low alloy steel. Vacuum 177:109387. https://doi.org/10.1016/j.vacuum.2020.109387

[26] He LJ, Manshadi AD, Dippenaar RJ (2012) The evolution of microstructure of Ti–6Al–4V alloy during concurrent hot deformation and phase transformation. Mater Sci Eng A 549:163-167. https://doi.org/10.1016/j.msea.2012.04.025

[27] Wang SG, Wu XQ (2012) Investigation on the microstructure and mechanical properties of Ti–6Al–4V alloy joints with electron beam welding. Mater Des 36:663-670. https://doi.org/10.1016/j.matdes.2011.11.068

[28] Won JW, Park CH, Hong SG, Lee CS (2015) Deformation anisotropy and associated mechanisms in rolling textured high purity titanium. J Alloy Compd 651:245-254. https://doi.org/10.1016/j.jallcom.2015.08.075

[29] Lathabai S, Jarvis BL, Barton KJ (2001) Comparison of keyhole and conventional gas tungsten arc welds in commercially pure titanium. Mater Sci Eng A 299:81-93. https://doi.org/10.1016/S0921-5093(00)01408-8.

[30] Baufeld B, Brandl E, Vander BO (2011) Wire based additive layer manufacturing: comparison of microstructure and mechanical properties of Ti-6Al-4V components fabricated by laser-beam deposition and shaped metal deposition. J Mater Process Technol 211:1146-1158. https://doi.org/10.1016/j.jmatprotec.2011.01.018

[31] Brandl E, PalmF, MichailovV, Viehweger B, Leyens C (2011) Mechanical properties of additive manufactured titanium (Ti-6Al-4V) blocks deposited by a solid-state laser and wire. Mater Des 32:4665-4675. https://doi.org/10.1016/j.matdes.2011.06.062.

[32] Carroll BE, PalmerTA, Beese AM (2015) Anisotropic tensile behavior of Ti-6Al-4V components fabricated with directed energy deposition additive manufacturing. Acta Mater 87:309-320. https://doi.org/10.1016/j.actamat.2014.12.054

[33] Keist JS, PalmerTA (2016) Role of geometry on properties of additively manufactured Ti-6Al-4V structures fabricated using laser based directed energy deposition. Mater Des 106:482-494. https://doi.org/10.1016/j.matdes.2016.05.045

[34] Kurz W, Fisher DJ (1984) Fundamentals of Solidification. Aedermannsdorf, Switzerland

[35] Rudlaff T, Dausinger F (1990) Increasing the efficiency of laser beam hardening. ICALEO 451:451-459. https://doi.org/10.2351/1.5058388

[36] Lv C, Ai YL, Yu QL, Chen WH, He W, Zhang JJ, Min XX (2018) Study on the growth kinetics of Al_2O_3 columnar crystal in Al_2O_3 matrix composite ceramics prepared by microwave sintering. J Cryst Growth 507:395-401. https://doi.org/10.1016/j.jcrysgro.2018.11.039